Journal of Materials Chemistry B

ROYAL SOCIETY OF CHEMISTRY

PAPER

View Article Online
View Journal | View Issue

Cite this: J. Mater. Chem. B, 2023, 11, 1044

Tumor-targeted molybdenum disulfide@barium titanate core–shell nanomedicine for dual photothermal and chemotherapy of triple-negative breast cancer cells†

Chandran Murugan, Hyoryong Lee and Sukho Park *

Combinational therapy can improve the effectiveness of cancer treatment by overcoming individual therapy shortcomings, leading to accelerated cancer cell apoptosis. Combinational cancer therapy is attained by a single nanosystem with multiple physicochemical properties providing an efficient synergistic therapy against cancer cells. Herein, we report a folate receptor-targeting dual-therapeutic (photothermal and chemotherapy) core–shell nanoparticle (CSNP) exhibiting a molybdenum disulfide core with a barium titanate shell (MoS_2@BT) to improve therapeutic efficacy against triple-negative breast cancer (TNBC) MDA-MB-231 cells. A simple hydrothermal approach was used to achieve the MoS_2@BT CSNPs, and their diameter was calculated to be approximately 180 ± 25 nm. In addition to improving the photothermal efficiency and stability of the MoS_2@BT CSNPs, their surface was functionalized with polydopamine (PDA) and subsequently modified with folic acid (FA) to achieve enhanced tumour-targeting CSNPs, named MoS_2@BT-PDA-FA (MBPF). Then, gemcitabine (Gem) was loaded into the MBPF, and its loading and releasing efficacy were calculated to be 17.5 wt% and 64.5 ± 3%, respectively. Moreover, the photothermal conversion efficiency (PCE) of MBPF was estimated to be 35.3%, and it also showed better biocompatibility, which was determined by an MTT assay. The MBPF significantly increased the ambient temperature to 56.3 °C and triggered Gem release inside the TNBC cells when exposed to a near-infrared (NIR) laser (808 nm, 1.5 W cm^{-2}, 5 min). Notably, the MoS_2@BT-based nanosystem was used as a photothermal agent and a therapeutic drug-loading container for combating TNBC cells. Benefiting from the combined therapy, MBPF reduced TNBC cell viability to 81.3% due to its efficient synergistic effects. Thus, the proposed tumour-targeting MoS_2@BT CSNP exhibits high drug loading, better biocompatibility, and improved anticancer efficacy toward TNBC cells due to its dual therapeutic approach in a single system, which opens up a new approach for dual cancer therapy.

Received 1st November 2022,
Accepted 17th December 2022

DOI: 10.1039/d2tb02382b

rsc.li/materials-b

1. Introduction

Increasing cancer incidence and mortality rates in recent years have made it one of the most terrible causes of death worldwide. Among cancers, triple-negative breast cancer (TNBC) has more aggressive clinical features, including rapid growth, high metastatic potential, poor prognosis, and high invasiveness. The forecast for TNBC is typically not as good as for other types.[1] Photothermal therapy (PTT) has been extensively researched and developed for breast cancer treatment as an emerging therapeutic approach. It is an essential alternative therapy that utilizes PTT agents to produce tremendous temperatures within the tumour cells after absorbing near-infrared (NIR) light.[2–4] Also, PTT is widely regarded as one of the most effective therapeutic strategies for combating tumours because of its high temporal specificity, affordability, noninvasiveness, remote controllability, and low side effects.[5,6] Despite these advantages, PTT alone has not produced more effective tumour therapy because of the uneven spreading of injected PTT agents and the difficulty of using NIR light to penetrate tumour tissues. Combination therapy, a therapeutic modality that combines PTT with other cancer therapies, can synergistically eradicate cancer cells.[7] In addition, conventional chemotherapy involves drugs that prevent cell proliferation and destroy cancer cells effectively. This approach is commonly used in tumour therapy; however, it is susceptible to drug resistance and severe side effects due to its poor drug specificity.[8] As a result, monotherapies, such as photothermal or chemotherapy alone, have several shortcomings when

Department of Robotics and Mechatronics Engineering, Multiscale Biomedical Robotics Laboratory, Daegu Gyeongbuk Institute of Science and Technology (DGIST), Daegu 42988, Republic of Korea. E-mail: shpark12@dgist.ac.kr

† Electronic supplementary information (ESI) available. See DOI: https://doi.org/10.1039/d2tb02382b

treating cancer cells. Combination therapy attributed to combining chemotherapy with hyperthermia, effectively resolves the limitations of monotherapies, increasing the efficacy of the therapy[9,10] because of its different mechanisms of action.[11] Thus, combination therapy offers an alternative, suitable mode of therapy that could significantly enhance the effectiveness of cancer treatment. In recent years, nanoparticle-mediated integration of chemotherapy with photothermal therapy has aroused increased interest in cancer treatment. An exciting aspect of combination therapy is that it is accomplished using a single nanosystem with different physicochemical properties, which improves synergistic cancer treatment. It is particularly beneficial to utilize hybrid components in a single nanosystem to provide multiple therapeutics/modalities as they combine the valuable features of both pure nanomaterials. Molybdenum disulfide (MoS_2) has gained increasing attention in the biomedicine field due to its large surface area and excellent biocompatibility, as well as its sulfur atoms, which play an important part in the formation and function of iron–sulfur proteins in the biological system. Its superior properties, such as a large internal band gap and high carrier mobility, allow for efficient photothermal conversion during PTT.[12] Moreover, MoS_2 nanoparticles (NPs) are an effective agent for direct tumour treatment with the added benefits of being tremendously flexible, able to undergo easy surface alteration with other elements, minimizing long-term toxicity, and rapidly degraded and removed from the body.[13] Therefore, MoS_2 nanomaterials serve as a platform material to create a multifunctional nanomedicine for cancer dual therapy by integration with other nanomaterials.[14,15]

Barium titanate (BT) is a talented piezoelectric material for biomedical applications due to its biological features, including high biocompatibility when contacting biological cells.[16,17] There has already been evidence that BT NPs are cytocompatible when incubated with mesenchymal stem cells (MSCs) at higher concentrations, such as 100 μg mL^{-1}.[18] Moreover, the role of poly(lactic-*co*-glycolic) acid/BT NPs in cell attachment and their effects on osteoblast and osteoclast differentiation or proliferation have also been demonstrated.[19] A previous report showed that BT NPs effectively deliver and enhance doxorubicin uptake by SH-SY5Y neuroblastoma cells.[20] Interestingly, BT NPs coated with gold can be used for photothermal therapy to treat cancerous lesions. In contrast, BT NPs coated with polymeric coatings can be used for gene delivery.[21] Hence, BT NPs have high potential to serve as a multi-purpose anticancer agent. Thus, fabricating a hybrid nanostructure using MoS_2 and BT may enhance the efficiency of a synergistic approach (PTT and chemotherapy) towards TNBC cells. In addition, a perfect nanocarrier has been outfitted with tumour-specific ligands, endowing the rapid uptake of nanomaterials inside cancer cells by significantly or strictly binding nanomaterials on target tumour cells. Tumour-targeting moieties, such as folic acid,[22] hyaluronic acid,[23] transferrin,[24] aptamer,[25] peptide,[26] and antibody,[27] have previously been utilized on the surface of drug delivery systems. A cell surface-anchored glycoprotein named folate receptor alpha (FR-α) is upregulated in several other sorts of epithelial cancers and 90% of ovarian carcinomas.[28,29] FR-α allows intracellular transport of folic acid (FA) conjugated nanocarrier *via* receptor-mediated endocytosis while binding FR-α with FA.[30] Due to its low expression in healthy tissues, FR-α has been proposed as an ideal candidate for tumour-targeted anticancer drug delivery.[31,32]

To the best of our knowledge, we report the first dual-therapeutic functional (photothermal agent and drug carrier) molybdenum disulfide (MoS_2) and barium titanate (BT) core–shell nanoparticles (MoS_2@BT CSNPs) for the synergistic therapy of MDA-MB-231 cells. The MoS_2@BT CSNPs were obtained *via a* one-step hydrothermal approach, followed by surface functionalization with polydopamine (PDA) to improve the PTT efficiency. To obtain the tumour-specific functionality, FA is functionalized on the surface of MoS_2@BT-PDA, named MoS_2-BT-PDA-FA (MBPF). MBPF with FA can bind to the highly expressed FR-α on most tumour cells and improve the accumulation of CSNPs at the tumour site. Then, gemcitabine (Gem), a deoxycytidine analogue, was loaded into the MBPF CSNPs to achieve chemotherapy with PTT. The MBPF increased the ambient temperature significantly to 56.3 °C and triggered Gem release inside the TNBC cells when exposed to a near-infrared (NIR) laser (808 nm, 1.5 W cm^{-2}, 5 min). Thus, the proposed tumour-targeted MoS_2@BT, an intelligent nanodrug system with different outlooks (core@shell) was used to attain PTT with chemotherapy in a single system against TNBC.

2. Materials and methods

2.1 Chemicals

Sodium molybdate dehydrates ($Na_2MoO_4{\cdot}2H_2O$, ≥99.5%), 1,1′-dioctadecyl-3,3,3′,3′-tetramethylindocarbocyanine perchlorate (DiR), barium carbonate ($BaCO_3$, ≥99%), thiourea (CH_4N_2S, ≥99%), titanium(IV) isopropoxide (97%), polyvinylpyrrolidone (PVP, M_w 40 000), citric acid ($C_6H_8O_7$, ≥99.5%), 1-ethyl-3-(3-dimethyl aminopropyl) carbodiimide (EDC), dopamine hydrochloride, 4′,6-diamidino-2-phenylindole (DAPI), folic acid (≥97%), *N*-hydroxysuccinimide (NHS), ethanol, acridine orange (AO), propidium iodide (PI), 2′-7′-dichlorofluorescin diacetate (DCFH-DA, ≥97%), gemcitabine hydrochloride (≥98%), and tris–HCl buffer (pH 8.5) were purchased from Sigma-Aldrich.

2.2 Synthesis of MoS_2@BT CSNPs

A simple hydrothermal method was used to prepare the MoS_2@BT CSNPs in two steps by mixing the precursors at 180 °C for 6 h. In brief, 30 mg of $Na_2MoO_4{\cdot}2H_2O$, 50 mg of PVP, and 30 mg of thiourea were first dissolved in 25 mL of Milli-Q water, and, second, 30 mg of $BaCO_3$, 50 μg of titanium(IV) isopropoxide, and 100 mg of $C_6H_8O_7$ were dispersed in 20 mL of ethanol solution. Then, the second mixture was poured dropwise into the first solution under vigorous stirring for 30 min. The blended mixture was then poured into a Teflon-lined autoclave and heated at 180 °C for 6 h. Finally, the grey colour product was obtained by centrifugation at 12 000 rpm for 20 min, and the impurities were removed by frequent washing with 70% ethanol and Milli-Q water. The obtained MoS_2@BT CSNPs were vacuum-dried overnight at 60 °C and stored for further use.

2.3 Synthesis of MoS_2@BT-PDA CSNPs

To prepare PDA-coated MoS_2@BT CSNPs, 50 mg of MoS_2@BT CSNP was dispersed in 25 mL of 10 mM tris–HCl buffer (pH 8.5) consisting of 20 mg of dopamine·HCl and the reaction was left under stirring for 12 h at room temperature (RT). The final product was gathered by centrifugation at 10 000 rpm for 20 min and the product was washed several times with Milli-Q water and ethanol. Finally, the MoS_2@BT-PDA CSNPs were dried using an oven for further use.

2.4 Folic acid (FA) conjugated MoS_2@BT-PDA (MBPF) CSNPs

To get folic acid (FA) functionalized MoS_2@BT-PDA CSNPs, 5 mg of FA and 1 mg of EDC were dispersed in 10 mL of anhydrous ethanol, and then 30 mg of MoS_2@BT-PDA in Milli-Q water was added dropwise to the mixture and it was stirred in the dark for 12 h at RT to get FA-functionalized MoS_2@BT-PDA, named MBPF CSNPs. Finally, the product was obtained by centrifugation at 12 000 rpm for 20 min, and the impurities were then removed by repeatedly washing the precipitate with 70% ethanol and Milli-Q water. The MBPF was vacuum-dried overnight at 60 °C and stored for further use.

2.5 Gemcitabine-loaded MBPF CSNPs

The gemcitabine (Gem) loading and release efficiency of MBPF CSNPs were investigated by the dialysis bag method. Briefly, 10 mg of MBPF CSNPs were dissolved in 5 mL of Gem aqueous solution (2 mg mL^{-1}); after mild stirring for 12 h, the Gem-loaded MBPF CSNPs were gathered by a centrifugation process (12 000 rpm, 10 min) and unloaded Gem was removed by washing twice with deionized water. The supernatant was measured before and after Gem loading at 270 nm to determine the drug loading capability of MBPF using a UV-visible spectrometer. The Gem encapsulation efficiency (EE) and loading content (LC) in MBPF were stated based on the following formulas:[33]

$$\mathrm{EE}(\%) = \frac{\text{Weight of Gem in MBPF}}{\text{Weight of the feeding Gem}} \times 100$$

$$\mathrm{LC}(\%) = \frac{\text{Weight of loaded Gem in MBPF}}{\text{Total weight of MBPF}} \times 100$$

2.6 Materials characterization

The core–shell structure, size, morphology, elemental mapping, and composition were determined with a high-resolution electron microscope (HR-TEM, Hitachi/HF-3300). X-ray diffraction (XRD) was utilized to assess the CSNP crystal structure (Panalytical/Empyrean, XRD) and the Fourier-transform infrared (FT-IR) spectrum was recorded using an FT-IR spectrometer (Thermo Scientific/Nicolet Continuum). The atomic valence states and the composition of MoS_2@BT were confirmed by X-ray photoelectron spectroscopy (XPS). Then, the UV-visible absorption spectrum of CSNPs was accessed using a nanodrop spectrophotometer (DS-11+, DeNovix, USA). Dynamic light scattering (DLS) was used to assess the size distribution and stability of MBPF (Wyatt Technology/DynaPro NanoStar). Filtered 100 μL of MBPF solution was used in a microcuvette to determine the size and stability of CSNPs. Triplicate experiments were investigated for each MPBF sample, and then the result was processed using DTS software version 3.32. A UV-vis-NIR spectrophotometer was utilized to assess the optical properties of MBPF, and the spectrum was recorded within the range of 300–900 nm using Agilent Technologies/Cary 5000 UV-Vis-NIR.

2.7 Drug release experiment

To investigate the release profile of Gem from MBPF, Gem-loaded MBPF CSNPs (2 mg) were dissolved into the dialysis bag and immersed into 10 mL phosphate buffer saline (PBS) solutions of different pH (5.0 or 7.4) and incubated at 37 °C for 24 h. At predetermined intervals, 200 μL of the PBS was removed from the medium, and the original volume was replenished with fresh PBS solution. The Gem discharged from MBPF was calculated by measuring the supernatant at 270 nm using a UV-visible spectrophotometer.

2.8 *In vitro* photothermal efficacy of MoS_2@BT and MBPF CSNPs

Cuvettes containing 300 μL aqueous dispersions of MBPF with diverse concentrations (25, 50, 75, and 100 μg mL^{-1}) were exposed to an NIR laser of 808 nm (1.5 W cm^{-2}) for 5 min and compared with distilled water (control experiment). Then, the heat-producing capacity of MBPF was monitored every 20 seconds using a thermal infrared imager, and the photothermal stability of MBPF CSNPs was evaluated with four cycles of on/off laser experiment to calculate the photothermal conversion efficiency (η), as reported previously.[34,35]

2.9 Cell culture for photothermal therapy

A 25 cm^2 tissue culture dish containing 5 mL of DMEM medium, 10% FBS, 100 μg mL^{-1} streptomycin, and 100 μg mL^{-1} penicillin was utilized to grow MDA-MB-231 cells at 37 °C using a humidified incubator supplied with 5% CO_2 gas. Then, the cells were grown until they reached cell confluency (80–85%) and rinsed three times with PBS solution. Finally, the MDA-MB-231 cells were harvested using 0.25% trypsin-EDTA for further experiments.

2.10 *In vitro* cytotoxicity test

A thiazolyl tetrazolium (MTT) assay was used to quantitatively evaluate the cell viability of MDA-MB-231 cells after incubation with saline, MoS_2@BT, MoS_2@BT-PDA, MBPF, MBPF + NIR, MBPF + Gem, and MBPF + Gem + NIR (1 mg mL^{-1}). Briefly, MDA-MB-231 cells (2×10^5 cells per well) were grown in 96-well plates for 24 h, then incubated with fresh medium containing different concentrations of CSNPs (5–100 μg mL^{-1}) and further cultured for 12 h, followed by NIR light irradiation (808 nm, 1.5 W cm^{-2}, 5 min) or not. After discarding the medium, 20 μL of MTT solution was supplied and incubated for a further 4 h. The formed formazan granules were defrosted in 200 μL of DMSO with gentle shaking, and the cell viability was measured

at 570 nm with a microplate reader using the following formula:

$$\text{Cell viability} = \frac{\text{OD of control sample} - \text{OD of test sample}}{\text{OD of control sample}} \times 100$$

2.11 *In vitro* synergistic antitumor efficacy of the CSNPs

The antitumor activity of the CSNPs was determined by a live/dead assay using AO/PI staining, respectively. The MBA-MD-231 cells (1×10^5 cells per well) were grown in a 12-well plate to reach confluency; then 100 μL of saline, MoS_2@BT, MBPF, MBPF + NIR, MBPF + Gem, and MBPF + Gem + NIR (1 mg mL^{-1}) was poured into each well and incubated for 12 h. Then, an NIR laser (808 nm, 1.5 W cm^{-2}) was used to irradiate each well with cells and washed with fresh PBS twice after 2 h of incubation. Finally, irradiated cells were stained with PI (10 mg mL^{-1}) and 50 μL of AO (10 mg mL^{-1}) for 15 min and then rinsed with fresh PBS three times. The stained MBA-MD-231 cells were visualized with a fluorescence microscope (LSM700, Zeiss).

2.12 *In vitro* ROS detection

Intratumor ROS generation was assessed by oxidation of DCFH-DA; MDA-MB-231 cells on a 12-well plate (1×10^5 cells per well) were incubated for 12 h at 37 °C. Afterwards, 100 μL of saline, MoS_2@BT, MBPF, MBPF + NIR, MBPF + Gem, and MBPF + Gem + NIR (1 mg mL^{-1}) was poured into each well and incubated for 12 h. Then, an NIR laser (808 nm, 1.5 W cm^{-2}) was used to irradiate each well with cells and washed with fresh PBS twice after 2 h of incubation. Then, the MDA-MB-231 cells were repeatedly rinsed with PBS after staining with DCFH-DA (30 μL, 1 mg mL^{-1}) for 15 min. The ROS generation capability

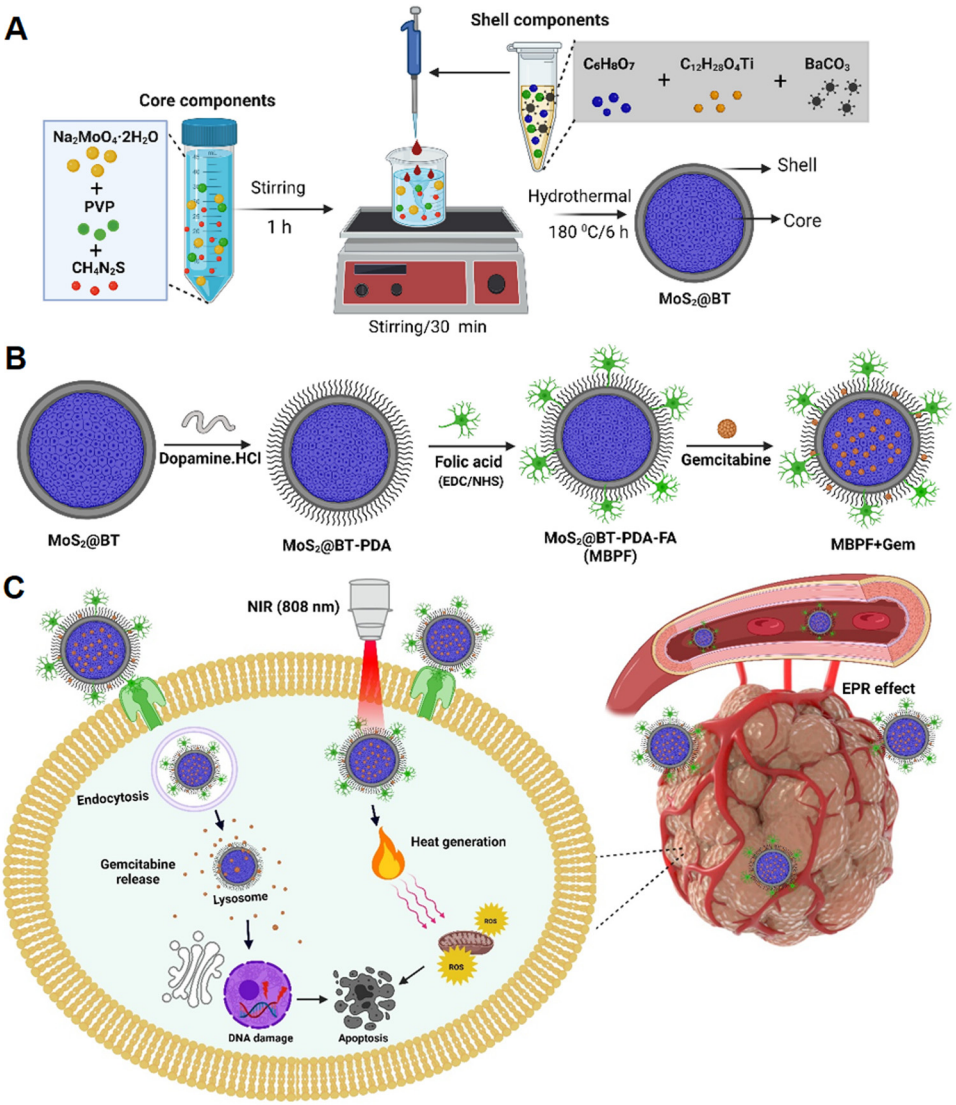

Scheme 1 (A and B) The schematic illustration shows the procedure for the formulation of MoS_2@BT and Gem-loaded MBPF CSNPs as a potent antitumor agent for combination chemo-photothermal therapy towards MDA-MB-231 cells and (C) the intracellular working machinery of Gem-loaded MBPF CSNPs when exposed to NIR laser irradiation (808 nm, 1.5 W cm^{-2}). By using enhanced permeability and retention (EPR) effects, MBPF passively targets MDA-MB-231 cells, causing a local temperature rise (>50 °C) within TNBC cells through their dual performance (chemo and PTT therapy).

of CSNPs was detected with a fluorescence microscope (LSM700, Zeiss), and DCF means the fluorescence intensity was calculated using emission and excitation wavelengths at 530 nm and 488 nm, respectively.[36]

2.13 Cellular uptake and antitumor efficacy of CSNPs

MBA-MD-231 cells (1×10^5 cells per dish) were seeded into a confocal dish with an appropriate growth medium and allowed to attach for 24 h. Then, MBA-MD-231 cells were treated with saline, MoS_2@BT, MBPF, MBPF + NIR, MBPF + Gem, and MBPF + Gem + NIR (1 mg mL^{-1}) and incubated for a further 12 h. Then, an NIR laser (808 nm, 1.5 W cm^{-2}) was used to irradiate each well with cells and washed with fresh PBS twice after 2 h of incubation. Then, the cells were stained with nuclear staining DAPI (blue) and membrane staining DiL (red) for 20 min and immediately washed several times with PBS. The stained MBA-MD-231 cells were pictured using a confocal laser scanning microscope (Olympus/FV1200).

2.14 Statistical analysis

Each result was obtained by three replicate experiments and displayed as means ± standard deviation (SD). Student's *t* test was applied to compare the data and significant variance was considered to be $^*p < 0.05$.

3. Results and discussion

The design, fabrication strategy, and surface modification of molybdenum disulfide@barium titanate (MoS_2@BT) core–shell nanoparticles (CSNPs) are shown in Scheme 1. MoS_2@BT CSNP was obtained by mixing the core-forming components ($Na_2MoO_4{\cdot}2H_2O$, PVP, and CH_4N_2S) with the shell-forming compositions ($C_{12}H_{28}O_4Ti$, $C_6H_8O_7$, and $BaCO_3$) at 180 °C for 6 h. A possible mechanism of MoS_2@BT CSNP formation can be stated as follows; the reduced Mo atom reacts with sulfur (S) to form MoS_2,[37] and then the PVP molecules are adsorbed into MoS_2 *via* chemical interactions between the Mo–S bond with either nitrogen atoms on the pyrrole ring or oxygen atoms on the carbonyl group of PVP, resulting in the formation of the core structure.[38] Moreover, the shell is formed by the activity of citric acid (CA), a molecule that possibly primarily produces BT phase-pure particles with tiny crystallite size and less clustered secondary particles.[39] Subsequently, the oxygen atom of the CA molecule in the shell components has the potential to react with the nitrogen atom of PVP in the core *via* hydrogen (O–H) bonding.[40,41] At high temperatures (180 °C), the burst nucleation and growth of significant numbers of BT crystal nuclei on the surface of MoS_2 form a shell structure. PVP and CA act as linker molecules between MoS_2 (core) and BT (shell) and play a crucial role in forming the MoS_2@BT core–shell structure. Thus, the formed MoS_2@BT CSNPs exhibit different outlooks, like a dense core with a transparent shell, which can provide efficient PTT and chemotherapy in a single system.

As shown in Scheme 1(B), the as-prepared MoS_2@BT CSNPs were coated with a polydopamine layer (PDA) through self-polymerization in an aqueous alkaline solution. It is well known that PDA coatings on CSNPs provide excellent biocompatibility,[42] aqueous solubility, and substantial photothermal properties,[43] particularly in the near-infrared (NIR) region for PTT *in vivo*.[44] Then, the MoS_2@BT-PDA surface was functionalized with folic acid (FA) to enhance targeting functionality and improve long-term blood circulation. This was achieved by a covalent coupling reaction between the amino of FA and the carboxyl groups of PDA in the presence of EDC and NHS to form MoS_2@BT-PDA-FA (MBPF). Finally, gemcitabine (Gem) was loaded into MBPF CSNPs *via* diffusion; the process of drug delivery and the mode of action of Gem-loaded MBPF CSNPs when exposed to near-infrared (NIR) are illustrated in Scheme 1(C). The cellular uptake of MBPF by MDA-MB-231 cells is initially recognized by the folate receptor (FR), which is highly expressed in breast cancer cells. Following the entry of MBPF into the cytoplasm, it absorbs near-infrared (NIR) light and converts it into heat, and triggers drug release when exposed to NIR radiation (808 nm, 1.5 W cm^{-2}, 5 min). The Gem-loaded MBPF induces ROS generation, blockage of DNA elongation, and DNA damage when exposed to NIR light, resulting in TNBC cells undergoing apoptosis or cell death.

Fig. 1(A) and (B) show the structure and morphology of the synthesized MoS_2@BT CSNPs; the transmission electron microscopy (TEM) images show the particles possessed uniform morphology, a spherical shape, and a diameter of about 180 ± 25 nm. Fig. 1(C) and (D) show the CSNPs with a visible core–shell structure, characterized by an amorphous and less dense shell uniformly coated on the dense core structure with some crystal planes, indicating that a core–shell structure was formed. TEM investigation also revealed that the inner core was 178 ± 10 nm in diameter, followed by a shell of about 25 ± 2 nm in thickness. As shown in Fig. 1(E), energy-dispersive X-ray spectroscopy (EDX) mapping images showed the presence of different elements (Mo, S, Ba, Ti, and O) in the MoS_2@BT CSNPs. Interestingly, the core structure of CSNPs comprises Mo, S, and Ba elements, and the shell is composed of Ti and O. The atomic compositions of Mo, S, and Ba were higher at the core and decreased radically from the core to the shell, whereas a significant amount of Ti and O was observed in the shell of CSNPs. The EDS spectrum image (Fig. S1, ESI†) also confirmed the presence of Mo, S, Ba, Ti, and O elements in the MoS_2@BT CSNPs, which was further proof of the successful synthesis of CSNPs.

To obtain detailed evidence about the phase composition and crystal structure of MoS_2@BT, MoS_2@BT-PDA, and MBPF CSNPs, X-ray diffraction (XRD) was performed between 10° and 80°. In Fig. 1(F), the XRD pattern of MoS_2@BT showed the presence of MoS_2 and BT, and the peaks observed at 31.8°, 33.9°, 39.0°, 46.1°, 49.3°, and 59.0° correspond to (100), (101), (103), (006), (105), and (110), respectively, confirming the crystalline phase of MoS_2.[45,46] Furthermore, diffraction peaks were also observed at 22.0°, 31.4°, 38.6°, 44.9°, 50.6°, 55.9°, 65.4°, 69.9°, 74.4°, and 78.6° corresponding to the (100), (110), (111), (200), (210), (211), (220), (300), (310) and (311) phases of BT (JCPDS No. 31–0174), respectively, indicating the presence of both MoS_2 and BT in the CSNPs. In the XRD patterns of

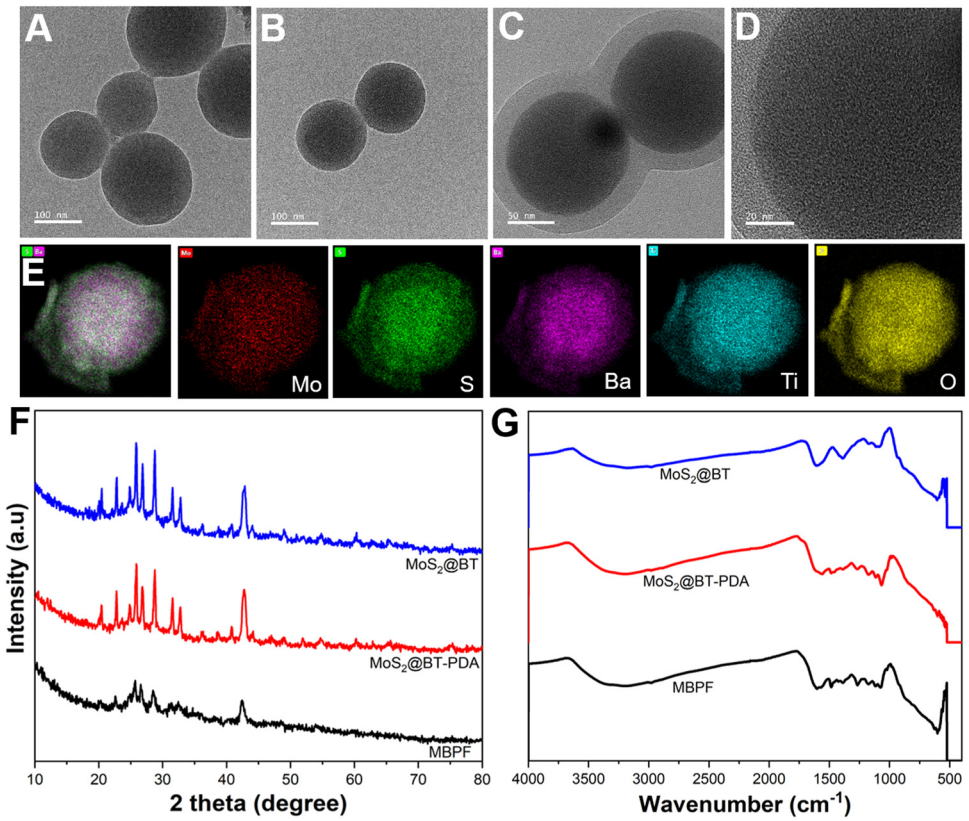

Fig. 1 Structure, morphological and chemical composition of CSNPs. TEM images of (A) and (B) the spherical-shaped group of CSNPs, (C) and (D) the morphology of the shell at higher magnification, (E) EDX mapping of MoS_2@BT CSNPs, (F) XRD and (G) FT-IR spectra of MoS_2@BT, MoS_2@BT-PDA, and MBPF CSNPs.

MoS_2@BT-PDA and MBPF CSNPs, all of the peaks match the crystalline structure of bare MoS_2@BT CSNPs with a lower degree of crystallinity, which indicates the incorporation of biomolecules such as PDA and FA in CSNPs, resulting in a slight decrease in absorption band intensity. These findings confirmed the existence of PDA and FA in the CSNP matrix.

The formation of MoS_2@BT, MoS_2@BT-PDA, MBPF CSNPs, and Gem-loaded MBPF CSNPs was confirmed by the UV-Vis spectrophotometer, as shown in Fig. S2, ESI.† FT-IR spectroscopy was recorded to observe the surface chemical structure and binding interaction of MoS_2@BT, MoS_2@BT-PDA, and MBPF CSNPs, as shown in Fig. 1(G). The broad absorption bands at 935, 1115, and 1602 cm^{-1} on MoS_2@BT CSNPs have been attributed to the stretching vibrations of S–S bond formation, hydroxyl groups, and Mo–O vibrations.[47] The peaks at 565 cm^{-1} and 1425 cm^{-1} correspond to Ti–O vibrations and bending vibrations of BT.[48,49] Also, the peaks between 1325 and 1385 cm^{-1} represent C–N and C═O of PVP.[50] The FT-IR spectrum of MoS_2@BT-PDA showed several new absorption peaks at 1608, 1557, and 1472 cm^{-1}, which correlated with the C═C vibration in the PDA benzene ring.[51,52] A peak revealed the C–O stretching vibration in PDA phenolic groups at 1268 cm^{-1} and the appearance of a new peak confirmed the effective coating of PDA on MoS_2@BT. The characteristic peaks of MBPF displayed at around 1635 and 1527 cm^{-1} correspond to the C═O (amide I band) and vibration of the N–H (2° amide) II band in MBPF.[53] The appearance of these peaks confirmed the conjugation of FA onto the surface of MBPF.

To characterize the atomic valence state and the composition of the MoS_2@BT CSNPs, X-ray photoelectron spectroscopy (XPS) was performed (Fig. 2). The XPS spectrum confirms the co-existence of Mo, S, Ba, Ti, and O elements in the MoS_2@BT CSNPs. As shown in Fig. 2(A), the XPS survey spectrum of MoS_2@BT confirmed the presence of Mo 3d, S 2p, Ba 3d, Ti 2p, and O 1s and revealed the coexistence of MoS_2 and BT in CSNPs.[54] Two bands at 229.2 eV (Mo $3d_{5/2}$) and 232.5 eV (Mo $3d_{3/2}$) correspond to Mo3d, as shown in Fig. 2(B). Also, the sulfur was confirmed by two peaks at 162.0 eV (S $2p_{3/2}$) and 163.3 eV (S $2p_{1/2}$), respectively, as depicted in Fig. 2(C). The binding energies of Mo and S were moderately similar to previously reported literature.[55] Moreover, the Ba 3d peak was divided into two parts (Ba $3d_{3/2}$ and Ba $3d_{5/2}$), where the Ba $3d_{5/2}$ peak at 778.78 eV and the Ba $3d_{3/2}$ peak at 794.23 eV confirmed the presence of barium in the BT shell.[56] There was a Ba 4d signal at 87.66 eV and a Ba 4p signal at 175.87 eV because of various barium orbitals in the BT shell (as observed in the survey spectrum), as shown in Fig. 2(D). In addition, two peaks of Ti $2p_{3/2}$ and Ti $2p_{1/2}$ were observed from the Ti 2p peak, and these peaks were separated into four peaks using Gaussian functions. Two of these peaks (Fig. 2(E)) were shown at about 457.25 eV and 463.59 eV corresponding to Ti $2p_{3/2}$ and Ti $2p_{1/2}$ peaks of Ti^{4+} in the BT shell, whereas the other two

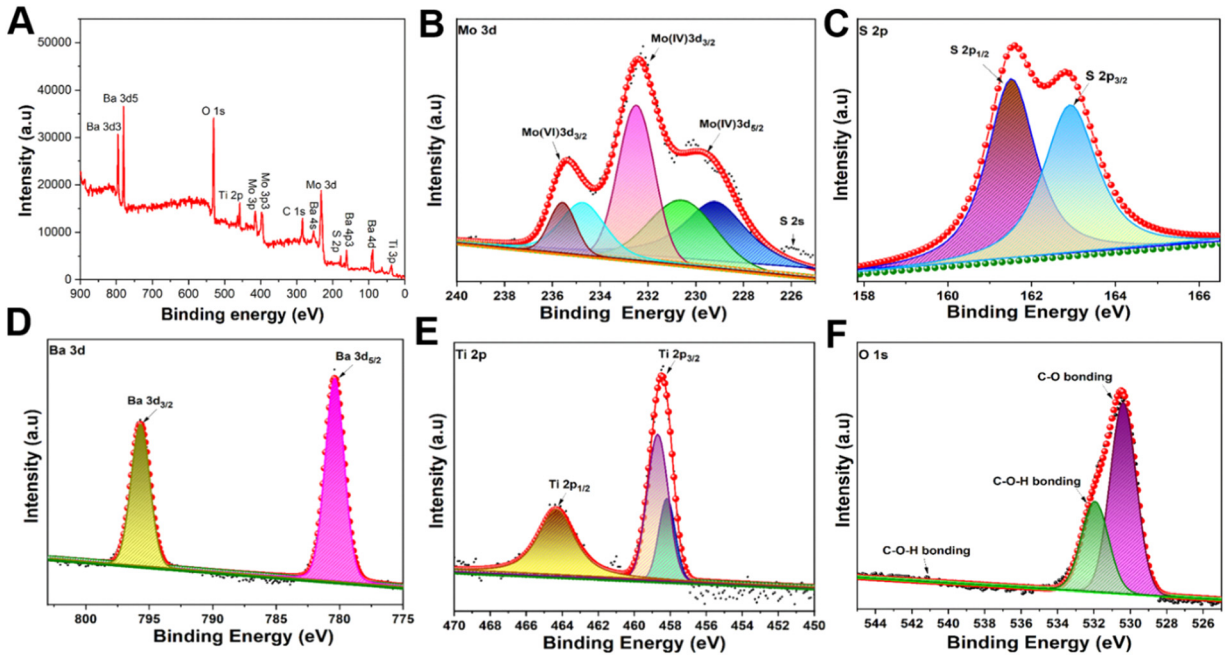

Fig. 2 High-resolution XPS spectra of MoS_2@BT CSNPs. (A) MoS_2@BT CSNPs survey spectrum, (B) spectra for the Mo 3d and S 2s of MoS_2, (C) spectra for the S 2p orbits of MoS_2, (D) spectra for the Ba 3d of BT, (E) spectra for the Ti 2p of BT and (F) spectra for the O 1s of BT.

peaks, Ti $2p_{3/2}$ and Ti $2p_{1/2}$ of Ti^{3+} in the BT shell were positioned around 456.39 eV and 462.18 eV, respectively.[57] The appearance of the O 1s spectrum (Fig. 2(F)) was split into two peaks at around 530.69 eV and 532.68 eV, which confirmed the presence of oxygen atoms in the form of Ba–O–Ti and Ti–O–Ti, respectively.[58] A peak representing C 1s was observed in the survey spectra, possibly due to CO_2 in the air (Fig. S3, ESI†). Also, the Mo 3d and S 2p peaks shifted their binding energies about 0.9 eV towards the lower energy direction, whereas Ba 3d, Ti 2p, and O 1s shifted their binding energies about 0.5 eV towards the higher energy direction. The shift of the peaks attributed to the interaction between MoS_2 and BT[59,60] indicates the successful formation of MoS_2@BT CSNPs. Dynamic light scattering (DLS) displayed the average hydrodynamic diameter of the MBPF CSNPs, which was calculated to be 205 ± 5 nm at 25 °C (Fig. S4, ESI†). No noticeable alteration in the hydrodynamic diameter of MBPF CSNPs was observed over a week and the average hydrodynamic diameter of the MBPF CSNPs was noted as 210 ± 3 nm by DLS at 25 °C, which demonstrated the considerable stability of the CSNPs (Fig. S5, ESI†). The UV-vis-NIR absorbance spectra were utilized to recorded the optical performance of MBPF (Fig. S6, ESI†). The absorption peak of MBPF was seen at around 350 nm, and broad absorption in the wavelength range of 800–820 nm.

The loading of Gem into CSNPs is based on electrostatic interaction. Hydrophilic Gem was loaded into the core and shell of MBPF CSNPs, and the Gem loading content of MBPF was calculated to be 17.5 wt%. The pH-responsiveness and NIR-laser activation release of Gem from MBPF CSNPs were investigated by the dialysis bag method for 24 h at different pH (5.0 and 7.4) that resemble the mature endosomes of tumour cells and normal physiological conditions, respectively. The amount of Gem discharged from MBPF CSNPs into the medium was evaluated by measuring the supernatant at 270 nm using UV-vis at given time intervals. Without laser irradiation, Gem release from MBPF CSNPs was slightly improved from 7 ± 2 to 53.9 ± 5% when the pH was adjusted from 7.4 to 5.0, as shown in Fig. 3(A). The pH-dependent discharge of Gem was due to improved solubility at lower pH levels, while the temperature-triggered discharge of Gem can be attributed to enhanced molecular motion at the higher temperature. Gem release was increased (64.5 ± 3%) at pH 5 with NIR laser irradiation compared with pH 5.0 without laser irradiation (<12%). Due to the lower pH of tumours (pH = 5.0–6.0) than normal tissue, the acidic condition of the tumour stimulates Gem release from MBPF CSNPs only at the tumour site. In addition, MBPF absorbs near-infrared (NIR) light and converts it into heat that kills tumour cells and enhances Gem release discharge, leading to an efficient synergistic antitumor effect. Gemcitabine is a pyrimidine nucleoside antimetabolite and has proven to be a promising new cytotoxic agent against numerous tumour types, including pancreatic, non-small cell lung, breast, and bladder cancer.[61–64] The released Gem may cause chain termination, blockage of DNA elongation, and suppress the TNBC cell proliferation, resulting in apoptosis.[65]

In Fig. 3(B), the photothermal conversion efficiency (PCE) of MBPF CSNPs was assessed by exposing 0.4 mL aqueous solutions of MBPF CSNPs with diverse concentrations (0, 25, 50, 75, and 100 μg mL^{-1}) to NIR irradiation (808 nm, 1.5 W cm^{-2}, 5 min) and recording consistent temperature changes using a thermal infrared camera. When MBPF CSNPs were used at a higher concentration (100 μg mL^{-1}), the temperature rose from 26 to 56.3 °C after NIR irradiation; in contrast, MBPF CSNPs with concentrations of 25, 50, and 75 μg mL^{-1} caused temperature

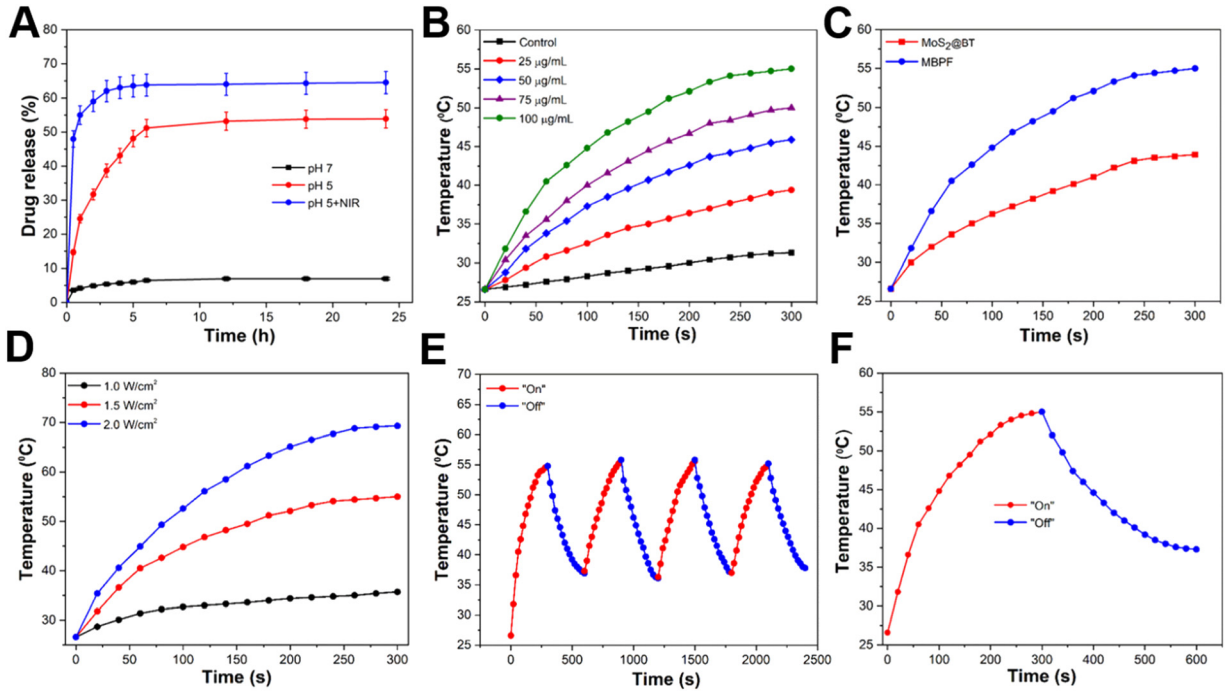

Fig. 3 (A) pH and NIR-based gemcitabine release from MBPF CSNPs. (B) Temperature rise curves of distilled water (control) and MBPF CSNPs under changing concentrations (0–100 μg mL^{-1}) when exposed to NIR laser irradiation (808 nm, 1.5 W cm^{-2}, 5 min). (C) Temperature increase curves of MoS_2@BT and MBPF CSNPs (100 μg mL^{-1} of concentration) with NIR irradiation. (D) Temperature increase of 100 μg mL^{-1} of MBPF CSNPs with NIR irradiation for 300 s at different power densities. (E) Four and (F) single rounds of NIR irradiation with on/off cycling for 600 s intervals.

increases from 26 °C to 39.4, 45.9, and 50.1 °C, respectively. Moreover, MBPF CSNPs exhibit concentration-dependent photothermal conversion behaviour, and their PCE was calculated to be about 35.3%, which is higher than those of MoS_2-PEG nanoflakes (27.6%) or MoS_2-chitosan (MoS_2-CS) nanosheets (24.4%).[66,67] The distilled water group displayed no significant temperature rise (3.1 °C), demonstrating that NIR irradiation did not harm normal tissue. The photothermal effect produced by MBPF CSNPs was potent and sufficient to thermally damage cancer tissues, thus making it a desirable candidate for effective PTT due to its excellent PCE performance. In Fig. 3(C), by exposing the CSNPs to an NIR laser (808 nm, 1.5 W cm^{-2}, 5 min), the heat generation performances of MoS_2@BT and MBPF CSNPs were observed to be 43.9 and 56.3 °C, respectively. There was an increase in heat generation by MBPF due to the PDA coating, which increased the ability to absorb photons more efficiently compared to MoS_2@BT.[68,69] Linear fitting of the MBPF sample solution showed an excellent linear relationship with an *R*-squared value of 0.9948, as shown in Fig. S7 (ESI†).[70] Fig. 3(D) illustrates a temperature increase of 100 μg mL^{-1} of MBPF CSNPs after laser radiation at 1, 1.5, and 2 W cm^{-2} power density for 5 min. The findings revealed that an obvious laser-power-dependent photothermal outcome was noted, and the temperature of the solution reached 69.3 °C at 2 W cm^{-2} laser irradiation, compared with 1 W cm^{-2} (35.7 °C) and 1.5 W cm^{-2} (56.3 °C) laser irradiation, respectively. A periodic NIR laser on/off control was used to show the photostability of MBPF CSNPs, in which 300 μL of MBPF CSNPs solution was irradiated using NIR laser light for 5 min, then cooled to room temperature without further exposure to NIR laser light. Fig. 3(E) shows no potential temperature decrease after four cycles of laser on/off irradiation. In Fig. 3(F), after removal of the laser, the solution of MBPF CSNPs was rapidly cooled, revealing exceedingly effective thermal conductivity. Therefore, the synthesized MBPF CSNPs demonstrated good photothermal stability under laser irradiation, indicating they are a potential candidate in cancer PTT therapy.

The MDA-MB-231 cell viability after incubation with MoS_2@BT, MoS_2@BT-PDA, and MBPF for 24 h at different concentrations (5–100 μg mL^{-1}) was determined by an MTT assay (Fig. 4(A)). The obtained results displayed no apparent cytotoxicity of MoS_2@BT, MoS_2@BT-PDA, and MBPF toward TNBC cells, even at a higher concentration (100 μg mL^{-1}), and the cell viabilities were calculated to be 92.2 ± 3.6, 96 ± 2.5 and 97.3 ± 1.6%, respectively. Previous findings displayed that the formulated MoS_2 nanomaterials have more significant cytotoxic effects for both cancer and normal cell lines than MoS_2@BT CSNPs.[15] The highly biocompatible MoS2@BT-PDA was due to the coating of PDA, which physically and chemically resembles natural melanin. PDA has received significant research interest in biomedical fields due to its extraordinary biocompatibility, antioxidant activity, strong NIR absorption, and high PCE.[71,72] Also, PDA consists of catechol and amino groups, which makes it easier to functionalize on MoS_2@BT.[73] Significant phototoxicity was recorded as 31.8, and 39.8% to NIR laser (808 nm, 1.5 W cm^{-2}) irradiated cells treated with 100 μg mL^{-1} of MoS_2@BT and MBPF, respectively. There was a significant increase in phototoxicity, to 81.3%, after treatment with MBPF + Gem + NIR compared to MBPF + Gem (34.6%).

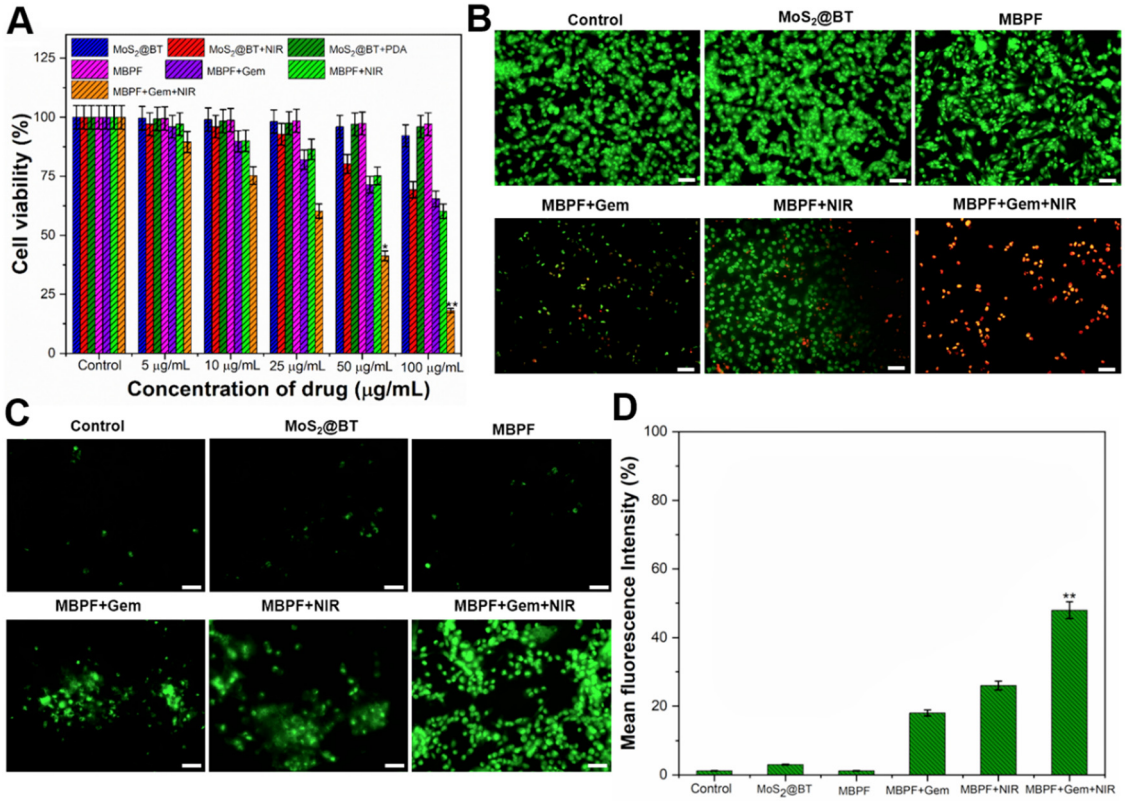

Fig. 4 (A) The MDA-MB-231 cell viability after treatment with different CSNPs for 24 h at various concentrations (5–100 μg mL^{-1}). (B) Fluorescence microscopic images of propidium iodide (PI)/acridine orange (AO) stained MDA-MB-231 cells after treatment with different CSNPs (100 μg mL^{-1}). (C) *In vitro* ROS-producing efficiency of different CSNPs (100 μg mL^{-1}) towards 2′,7′-dichlorofluorescein diacetate (DCFH-DA) stained MDA-MB-231 cells. (D) DCF fluorescence intensity was measured in CSNP-treated DCFH-DA stained MDA-MB-231 cells, which was proportional to ROS production. The data representing mean ± SD $^{**}p \leq 0.1$ was measured as statistically significant. Scale bar 50 μm.

As a result, the combined treatment effect was superior to that of photothermal therapy or chemotherapy alone. Then, the photothermal cytotoxicities of saline (control), MoS_2@BT, MBPF, MBPF + Gem, MBPF + NIR, and MBPF + Gem + NIR against MDA-MB-231 cells were explored by live/dead staining, as shown in Fig. 4(B). The stain AO, an intercalating dye, can stain both live and dying cells, whereas PI, an intercalating dye, can only penetrate the membranes of dead and dying cells. According to these findings, TNBC cells treated with saline, MoS_2@BT, and MBPF were shown to have more live cells (green fluorescence), but when treated with MBPF + Gem, minimal inhibition was observed. In addition, cells treated with MBPF + Gem + NIR exhibited higher cytotoxicity (81.3%) than Gem-loaded MBPF (34.6%) and MBPF + NIR (39.8%). A significant factor in this cytotoxicity was the ability of the FA on MBPF to bind specifically to the overexpressed folate receptor on MDA-MB-231 cells, leading to receptor-mediated endocytosis.[74,75] As a result of MBPF internalization, Gem was released into the cytoplasm, and NIR laser irradiation (808 nm, 1.5 W cm^{-2}) enhanced the therapeutic effect by combining chemo-photothermal therapy against MDA-MB-231 cells.

The intracellular ROS generation of different CSNPs was examined against DCFH-DA stained MDA-MB-231 cells after exposure with or without an NIR laser (Fig. 4(C)). The cells treated with saline, MoS_2@BT and MBPF CSNPs groups showed no appropriate ROS generation and revealed the excellent biocompatibility of these nanomaterials. Also, MBPF + Gem treated cells showed moderate ROS production, which was caused by a significant amount of Gem released inside the TNBC cells. Moreover, MBPF + Gem + NIR induced an increased amount of ROS generation in MDA-MB-231 cells; the appropriate ROS generation was noted due to the dual therapeutic performance (PTT and chemotherapy) of MBPF. The ROS level in MDA-MB-231 cells after treatment with different CSNPs was examined using a fluorescence plate reader (Fig. 4(D)). The cells treated with MBPF + Gem + NIR displayed higher ROS levels compared to other treated groups. Efficient combinational therapy was achieved due to the massive entry of MBPF into the cytoplasm. MBPF absorbs NIR light and converts it to heat, as well as triggering Gem release inside the TNBC cells when exposed to NIR radiation (808 nm, 1.5 W cm^{-2}, 5 min). MBPF with unique characteristics plays an essential role in relocating the produced thermal energy to the surrounding TNBC cell matrix, leading to an increase in the temperature up to <56 °C and it causes the production of peroxides, hydroxyl radicals, and singlet oxygen by oxidizing essential cellular macromolecules. The increased intracellular temperature also alters the functions of enzymatic proteins and many structural proteins

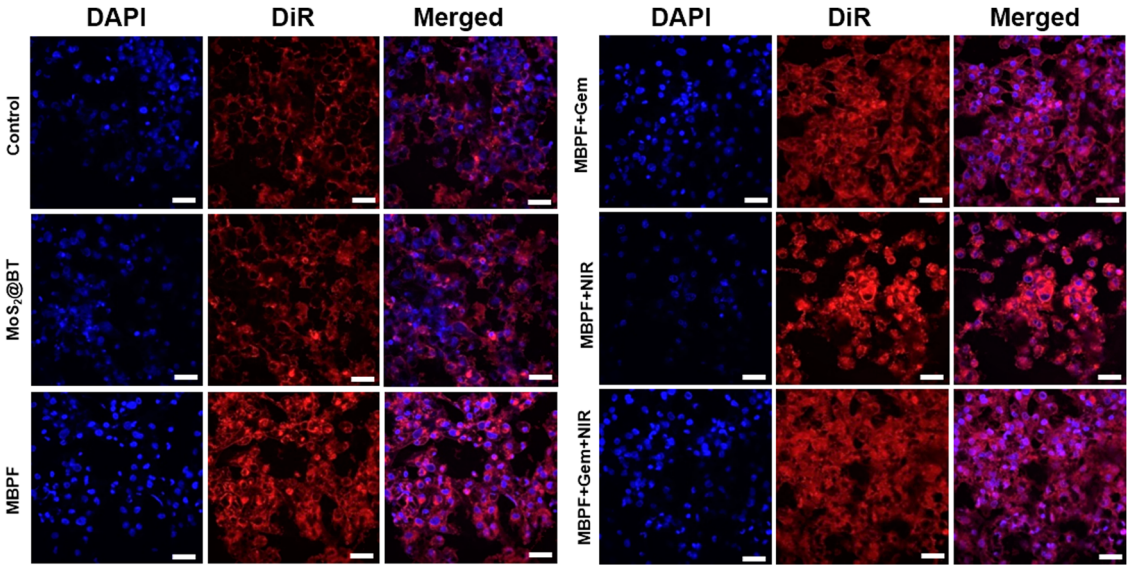

Fig. 5 Cellular uptake and antitumor activity of CSNPs were determined by confocal laser scanning microscopy (CLSM). The uptake of DAPI and DiR-stained MDA-MB-231 cells treated with various forms of CSNPs after exposure with or without NIR laser was observed for 24 h. Scale bar 25 μm.

within the cellular organelles like mitochondria and nucleus of TNBC cells and causes them to have increased sensitivity to heat.[76] In particular, mitochondrial membrane elements are incredibly vulnerable to ROS-induced oxidative damage. Unsaturated fatty acids are hugely present in the phospholipid compositions of mitochondrial membrane, which are potentially susceptible to oxygen radical attack due to the occurrence of a double bond that undergoes peroxidation through a series of oxidative reactions. Hence, ROS play a vital part as intracellular mediators of heat-induced cytotoxicity and heat-induced oxidative stress.[77]

The FA-tethered MBPF binds explicitly with the overexpressed folate receptor alpha (FR-α) on MDA-MB-231 cells, leading to endocytosis of MBPF CSNPs.[74,75] A cell-surface-anchored glycoprotein FR-α is upregulated in several other types of epithelial cancers and 90% of ovarian carcinomas.[28,29,78] FR-α allows intracellular transport of FA-tethered MBPF *via* receptor-mediated endocytosis while binding FR-α with FA.[30] As shown in Fig. 5, MoS_2@BT, MBPF, MBPF + Gem, MBPF + NIR, and MBPF + Gem + NIR CSNPs incubated with MDA-MB-231 cells, followed by exposure to an NIR laser or not to assess the uptake efficacy of different CSNPs by CLSM. The cellular uptake and anti-tumour effectiveness were determined by DiR and DAPI stain, in which DiR was used to track the distribution of CSNPs inside the cancer cells, and DAPI was utilized to evaluate the number of nuclei and gross cell structure of TNBC cells. The red fluorescent intensity (DiR) was lower in control and MoS_2@BT treated groups, indicating no appropriate uptake and no inhibitory effects on MDA-MB-231 cells. The red fluorescence intensity of the cytoplasm was more vigorous after treatment with MBPF, MBPF + Gem, MBPF + NIR, and MBPF + Gem + NIR CSNPs, which is due to the functionalization of nanomaterials with FA. Furthermore, MDA-MB-231 cells treated with MBPF + Gem + NIR CSNPs showed increased red fluorescence with irregular cellular morphology, causing complete damage to the nucleus and mitochondria due to the combined treatment effect (PTT and chemotherapy) of MBPF when exposed to NIR laser irradiation, leading to the death of cancer cells. Thus, the designed MBPF nanomedicine can effectively reach the TNBC cells through the EPR effect, whereas the biomolecule (FA) conjugated at the MBPF surface allows active targeting by the interaction of FA with overexpressed FR-α of breast cancer cells for an effective combinational (PTT/chemotherapy) approach.

4. Conclusion

In conclusion, we have demonstrated the preparation of a surface-modified MoS_2@BT core–shell nanomedicine for combinational (PTT and chemotherapy) against triple-negative breast cancer (TNBC) cells. A simple hydrothermal approach was used to synthesize the MoS_2@BT CSNPs, and its diameter was calculated to be approximately 180 ± 20 nm. The polydopamine (PDA) was functionalized on the MoS_2@BT surface to achieve MoS_2@BT-PDA nanomedicine by *in situ* polymerization and further modified with folic acid (FA) to obtain a tumour-functionality nanocomposite named MoS_2@BT-PDA-FA (MBPF). Then, the chemotherapeutic drug gemcitabine (Gem) was loaded onto MBPF CSNPs, ultimately producing the nanodrug system in an easily-operated way. The prepared MBPF CSNPs exhibit favourable biocompatibility and realized the tissue-specific delivery of gemcitabine at the tumour microenvironment (pH 5.0–6.0). Then, Gem loading and release efficacy were calculated to be 17.5 wt% and 64.5 ± 3%, respectively. Moreover, the photothermal conversion efficiency (PCE) of MBPF was estimated to be 35.3%, and it also showed better biocompatibility which was determined by an MTT assay. The MBPF increased ambient temperature significantly to

56.3 °C and triggered Gem release inside the TNBC cells when exposed to a near-infrared (NIR) laser (808 nm, 1.5 W cm^{-2}, 5 min). Cellular uptake of MBPF by MDA-MB-231 cells was also confirmed by a confocal microscopy study, and the internalized MBPF induced blockage of DNA elongation, ROS generation, and DNA damage in the TNBC cells when the cells were exposed to NIR irradiation. These findings support the therapeutic properties of MoS_2@BT CSNPs, and the dual therapeutic approach of MBPF with excellent clinical outcomes opens up a new strategy for combating cancer.

Author contributions

Chandran Murugan: conceptualization, data curation, writing-original draft, validation, methodology. Hyoryong Lee: conducted data analysis and co-revised the manuscript, and Sukho Park: funding acquisition, writing–review & editing, supervision.

Conflicts of interest

There are no conflicts to declare.

Acknowledgements

This work was supported by the National Research Foundation (NRF), funded by the Ministry of Science and ICT (NRF-2021R1A2C3007817).

References

1 L. Yin, *et al.*, Triple-negative breast cancer molecular subtyping and treatment progress, *Breast Cancer Res.*, 2020, **22**(1), 1–13.
2 L. Cheng, *et al.*, Functional nanomaterials for phototherapies of cancer, *Chem. Rev.*, 2014, **114**(21), 10869–10939.
3 J. Li, *et al.*, Near Infrared Photothermal Conversion Materials: Mechanism, Preparation and Photothermal Cancer Therapy Applications, *J. Mater. Chem. B*, 2021, **9**, 7909–7926.
4 L. Zou, *et al.*, Current approaches of photothermal therapy in treating cancer metastasis with nanotherapeutics, *Theranostics*, 2016, **6**(6), 762.
5 R. Xiong, *et al.*, Photothermal nanofibres enable safe engineering of therapeutic cells, *Nat. Nanotechnol.*, 2021, **16**(11), 1281–1291.
6 H. Dai, *et al.*, Boron difluoride formazanate dye for high-efficiency NIR-II fluorescence imaging-guided cancer photothermal therapy, *Chin. Chem. Lett.*, 2022, **33**(5), 2501–2506.
7 S. Su, *et al.*, Integration of photothermal therapy and synergistic chemotherapy by a porphyrin self-assembled micelle confers chemosensitivity in triple-negative breast cancer, *Biomaterials*, 2016, **80**, 169–178.
8 J. Nam, *et al.*, Chemo-photothermal therapy combination elicits anti-tumor immunity against advanced metastatic cancer, *Nat. Commun.*, 2018, **9**(1), 1–13.
9 C. Murugan, *et al.*, Two-dimensional cancer theranostic nanomaterials: Synthesis, surface functionalization and applications in photothermal therapy, *J. Controlled Release*, 2019, **299**, 1–20.
10 C. Murugan and S. Park, Cerium Ferrite@Molybdenum Disulfide Nanozyme for Intracellular ROS Generation and Photothermal-Based Cancer Therapy, *J. Photochem. Photobiol., A*, 2022, 114466.
11 Z. Deng, *et al.*, Nanomaterial-mediated platinum drug-based combinatorial cancer therapy, *View*, 2021, **2**(1), 20200030.
12 J. Wang, *et al.*, MoS_2-based nanocomposites for cancer diagnosis and therapy, *Bioact. Mater.*, 2021, **6**(11), 4209–4242.
13 L. Chen, *et al.*, Facile synthesis of novel albumin-functionalized flower-like MoS_2 nanoparticles for *in vitro* chemo-photothermal synergistic therapy, *RSC Adv.*, 2016, **6**(16), 13040–13049.
14 R. Sha and T. K. Bhattacharyya, MoS_2-based nanosensors in biomedical and environmental monitoring applications, *Electrochim. Acta*, 2020, **349**, 136370.
15 C. Murugan, *et al.*, Nanoceria decorated flower-like molybdenum sulphide nanoflakes: an efficient nanozyme for tumour selective ROS generation and photo thermal therapy, *Chem. Commun.*, 2019, **55**(55), 8017–8020.
16 C. Shuai, *et al.*, A strawberry-like Ag-decorated barium titanate enhances piezoelectric and antibacterial activities of polymer scaffold, *Nano Energy*, 2020, **74**, 104825.
17 E. Prokhorov, *et al.*, Chitosan–$BaTiO_3$ nanostructured piezopolymer for tissue engineering, *Colloids Surf., B*, 2020, **196**, 111296.
18 G. Ciofani, *et al.*, Effects of barium titanate nanoparticles on proliferation and differentiation of rat mesenchymal stem cells, *Colloids Surf., B*, 2013, **102**, 312–320.
19 G. Ciofani, L. Ricotti and V. Mattoli, Preparation, characterization and *in vitro* testing of poly(lactic-*co*-glycolic) acid/barium titanate nanoparticle composites for enhanced cellular proliferation, *Biomed. Microdevices*, 2011, **13**(2), 255–266.
20 G. Ciofani, *et al.*, Barium titanate nanoparticles: highly cytocompatible dispersions in glycol-chitosan and doxorubicin complexes for cancer therapy, *Nanoscale Res. Lett.*, 2010, **5**(7), 1093–1101.
21 G. G. Genchi, *et al.*, Barium titanate nanoparticles: promising multitasking vectors in nanomedicine, *Nanotechnology*, 2016, **27**(23), 232001.
22 T. Anirudhan and S. S. Nair, Polyelectrolyte complexes of carboxymethyl chitosan/alginate based drug carrier for targeted and controlled release of dual drug, *J. Drug Delivery Sci. Technol.*, 2019, **51**, 569–582.
23 W. Lin, *et al.*, Development of zwitterionic polypeptide nanoformulation with high doxorubicin loading content for targeted drug delivery, *Langmuir*, 2018, **35**(5), 1273–1283.
24 L. L. Israel, *et al.*, A combination of tri-leucine and angiopep-2 drives a polyanionic polymalic acid nanodrug platform across the blood–brain barrier, *ACS Nano*, 2019, **13**(2), 1253–1271.
25 G. K. Abou-Alfa, *et al.*, Randomized phase II placebo controlled study of codrituzumab in previously treated patients

with advanced hepatocellular carcinoma, *J. Hepatol.*, 2016, **65**(2), 289–295.
26 Z. W. Lim, *et al.*, Magnetically responsive peptide coacervates for dual hyperthermia and chemotherapy treatments of liver cancer, *Acta Biomater.*, 2020, **110**, 221–230.
27 A. Chall, *et al.*, Ablation of cells in mice using antibody-functionalized multiwalled carbon nanotubes (Ab-MWCNTs) in combination with microwaves, *Nanotechnology*, 2021, **32**(19), 195102.
28 A. Cheung, *et al.*, Targeting folate receptor alpha for cancer treatment, *Oncotarget*, 2016, **7**(32), 52553.
29 A. Kurosaki, *et al.*, Serum folate receptor alpha as a biomarker for ovarian cancer: Implications for diagnosis, prognosis and predicting its local tumor expression, *Int. J. Cancer*, 2016, **138**(8), 1994–2002.
30 Z. Hou, *et al.*, Dual targeting of epithelial ovarian cancer *via* folate receptor α and the proton-coupled folate transporter with 6-substituted pyrrolo [2,3-*d*] pyrimidine antifolates, *Mol. Cancer Ther.*, 2017, **16**(5), 819–830.
31 C. Yao, *et al.*, Folate receptor α regulates cell proliferation in mouse gonadotroph αT3-1 cells, *Exp. Cell Res.*, 2009, **315**(18), 3125–3132.
32 D. Paolino, *et al.*, Folate-targeted supramolecular vesicular aggregates as a new frontier for effective anticancer treatment in *in vivo* model, *Eur. J. Pharm. Biopharm.*, 2012, **82**(1), 94–102.
33 H. Xu, *et al.*, An efficient Trojan delivery of tetrandrine by poly(*N*-vinylpyrrolidone)-*block*-poly(ε-caprolactone)(PVP-*b*-PCL) nanoparticles shows enhanced apoptotic induction of lung cancer cells and inhibition of its migration and invasion, *Int. J. Nanomed.*, 2014, **9**, 231.
34 H. Lin, *et al.*, A two-dimensional biodegradable niobium carbide (MXene) for photothermal tumor eradication in NIR-I and NIR-II biowindows, *J. Am. Chem. Soc.*, 2017, **139**(45), 16235–16247.
35 P. An, *et al.*, Photothermal-enhanced inactivation of glutathione peroxidase for ferroptosis sensitized by an autophagy promotor, *ACS Appl. Mater. Interfaces*, 2019, **11**(46), 42988–42997.
36 C. Murugan, *et al.*, Combinatorial nanocarrier based drug delivery approach for amalgamation of anti-tumor agents in breast cancer cells: An improved nanomedicine strategy, *Sci. Rep.*, 2016, **6**(1), 1–22.
37 Y. Li, *et al.*, MoS_2 nanoparticles grown on graphene: an advanced catalyst for the hydrogen evolution reaction, *J. Am. Chem. Soc.*, 2011, **133**(19), 7296–7299.
38 W. Wang, *et al.*, PVP Functionalized Marigold-like MoS_2 as a New Electrocatalyst for Highly Efficient Electrochemical Hydrogen Evolution, *Electrocatalysis*, 2020, **11**(4), 383–392.
39 K. K. Lee, *et al.*, Preparation of nano-sized $BaTiO_3$ particle by citric acid-assisted spray pyrolysis, *J. Alloys Compd.*, 2005, **395**(1–2), 280–285.
40 P. Ramadoss, *et al.*, Low-cost and biodegradable cellulose/PVP/activated carbon composite membrane for brackish water treatment, *J. Appl. Polym. Sci.*, 2020, **137**(22), 48746.
41 S. Mallakpour and M. Naghdi, Fabrication and characterization of novel polyvinylpyrrolidone nanocomposites having SiO_2 nanoparticles modified with citric acid and L(+)-ascorbic acid, *Polymer*, 2016, **90**, 295–301.
42 P. Yan, *et al.*, The *in vitro* biomineralization and cytocompatibility of polydopamine coated carbon nanotubes, *Appl. Surf. Sci.*, 2011, **257**(11), 4849–4855.
43 Y. Liu, K. Ai and L. Lu, Polydopamine and its derivative materials: synthesis and promising applications in energy, environmental, and biomedical fields, *Chem. Rev.*, 2014, **114**(9), 5057–5115.
44 Y. Liu, *et al.*, Dopamine-melanin colloidal nanospheres: an efficient near-infrared photothermal therapeutic agent for *in vivo* cancer therapy, *Adv. Mater.*, 2013, **25**(9), 1353–1359.
45 T. S. Sahu and S. Mitra, Exfoliated MoS_2 sheets and reduced graphene oxide-an excellent and fast anode for sodium-ion battery, *Sci. Rep.*, 2015, **5**(1), 1–13.
46 X. Zhang, *et al.*, Facile synthesis and characterization of ultrathin MoS_2 nanosheets, *Mater. Lett.*, 2014, **130**, 83–86.
47 C. Murugan, *et al.*, Controlled decoration of nanoceria on the surface of MoS_2 nanoflowers to improve the biodegradability and biocompatibility in Drosophila melanogaster model, *Nanotechnology*, 2022, **33**(20), 205703.
48 C.-C. Li, *et al.*, Efficient hydroxylation of $BaTiO_3$ nanoparticles by using hydrogen peroxide, *Colloids Surf., A*, 2010, **361**(1–3), 143–149.
49 J. Mullens, *et al.*, The use of TGA-MS, TGA-FTIR, HT-XRD and HT-DRIFT for the preparation and characterization of $PbTiO_3$ and $BaTiO_3$, *Thermochim. Acta*, 2002, **392**, 29–35.
50 U. K. Bangi, *et al.*, Effects of successive additions of two capping ligands on the structural properties of PbO nanoparticles, *J. Nanopart. Res.*, 2013, **15**(11), 1–8.
51 N. Li, *et al.*, Enzyme-free fluorescent biosensor for the detection of DNA based on core–shell Fe_3O_4 polydopamine nanoparticles and hybridization chain reaction amplification, *Biosens. Bioelectron.*, 2016, **77**, 525–529.
52 X. Gao, *et al.*, Rapid and sensitive detection of Staphylococcus aureus assisted by polydopamine modified magnetic nanoparticles, *Talanta*, 2018, **186**, 147–153.
53 N. Andhariya, *et al.*, Folic acid conjugated magnetic drug delivery system for controlled release of doxorubicin, *J. Nanopart. Res.*, 2013, **15**(1), 1–12.
54 X.-R. Yu, *et al.*, Auger parameters for sulfur-containing compounds using a mixed aluminum–silver excitation source, *J. Electron Spectrosc. Relat. Phenom.*, 1990, **50**(2), 159–166.
55 Y. Chen, S. Lan and M. Zhu, Construction of piezoelectric $BaTiO_3/MoS_2$ heterojunction for boosting piezo-activation of peroxymonosulfate, *Chin. Chem. Lett.*, 2021, **32**(6), 2052–2056.
56 Y. Shi, *et al.*, Selective decoration of Au nanoparticles on monolayer MoS_2 single crystals, *Sci. Rep.*, 2013, **3**(1), 1–7.
57 C. Miot, *et al.*, X-ray photoelectron spectroscopy characterization of barium titanate ceramics prepared by the citric route. Residual carbon study, *J. Mater. Res.*, 1997, **12**(9), 2388–2392.
58 J.-L. Jou, *et al.*, The higher energy components in Ti2p Xps spectrum of Ga doped barium titanate, *Chin. J. Phys.*, 2012, **50**(6), 926–931.

59 Q. Yu, *et al.*, The dielectric and photochromic properties of defect-rich $BaTiO_3$ microcrystallites synthesized from Ti_2O_3, *Mater. Sci. Eng., B*, 2012, **177**(9), 639–644.
60 X. Zhao, *et al.*, Piezotronic effect of single/few-layers MoS_2 nanosheets composite with TiO_2 nanorod heterojunction, *Nano Energy*, 2019, **66**, 104168.
61 N. M. Cerqueira, P. A. Fernandes and M. J. Ramos, Understanding ribonucleotide reductase inactivation by gemcitabine, *Chem. – Eur. J.*, 2007, **13**(30), 8507–8515.
62 H. von der Maase, *et al.*, Gemcitabine and cisplatin versus methotrexate, vinblastine, doxorubicin, and cisplatin in advanced or metastatic bladder cancer: results of a large, randomized, multinational, multicenter, phase III study, *J. Clin. Oncol.*, 2000, **18**(17), 3068–3077.
63 Hr Burris, *et al.*, Improvements in survival and clinical benefit with gemcitabine as first-line therapy for patients with advanced pancreas cancer: a randomized trial, *J. Clin. Oncol.*, 1997, **15**(6), 2403–2413.
64 L. Crino, *et al.*, Gemcitabine and cisplatin versus mitomycin, ifosfamide, and cisplatin in advanced non–small-cell lung cancer: A randomized phase III study of the Italian Lung Cancer Project, *J. Clin. Oncol.*, 1999, **17**(11), 3522–3530.
65 C. Zhang, *et al.*, pn Heterojunction of BiOI/ZnO nanorod arrays for piezo-photocatalytic degradation of bisphenol A in water, *J. Hazard. Mater.*, 2020, **399**, 123109.
66 W. Feng, *et al.*, Flower-like PEGylated MoS_2 nanoflakes for near-infrared photothermal cancer therapy, *Sci. Rep.*, 2015, **5**(1), 1.
67 W. Yin, *et al.*, High-throughput synthesis of single-layer MoS_2 nanosheets as a near-infrared photothermal-triggered drug delivery for effective cancer therapy, *ACS Nano*, 2014, **8**(7), 6922–6933.
68 J. Carmichael, *et al.*, Advanced breast cancer: a phase II trial with gemcitabine, *J. Clin. Oncol.*, 1995, **13**(11), 2731–2736.
69 X. Zou, *et al.*, A Polydopamine-Coated Platinum Nanoplatform for Tumor-Targeted Photothermal Ablation and Migration Inhibition, *Front. Oncol.*, 2022, **12**, 860718.
70 Z. Huang, *et al.*, Radar-like MoS_2 nanoparticles as a highly efficient 808 nm laser-induced photothermal agent for cancer therapy, *RSC Adv.*, 2016, **6**(37), 31031–31036.
71 X. Wu, *et al.*, Localized heating with a photothermal polydopamine coating facilitates a novel membrane distillation process, *J. Mater. Chem. A*, 2018, **6**(39), 18799–18807.
72 C. Qi, *et al.*, Melanin/polydopamine-based nanomaterials for biomedical applications. Science China, *Chemistry*, 2019, **62**(2), 162–188.
73 X. Liu, *et al.*, Mussel-inspired polydopamine: a biocompatible and ultrastable coating for nanoparticles *in vivo*, *ACS Nano*, 2013, **7**(10), 9384–9395.
74 H. Lee, *et al.*, Mussel-inspired surface chemistry for multifunctional coatings, *Science*, 2007, **318**(5849), 426–430.
75 M. Fernández, F. Javaid and V. Chudasama, Advances in targeting the folate receptor in the treatment/imaging of cancers, *Chem. Sci.*, 2018, **9**(4), 790–810.
76 L. Yang, *et al.*, Photothermal therapeutic response of cancer cells to aptamer–gold nanoparticle-hybridized graphene oxide under NIR illumination, *ACS Appl. Mater. Interfaces*, 2015, **7**(9), 5097–5106.
77 D. M. Katschinski, *et al.*, Pivotal role of reactive oxygen species as intracellular mediators of hyperthermia-induced apoptosis., *J. Biol. Chem.*, 2000, **275**(28), 21094–21098.
78 Y.-L. Chen, *et al.*, Serous ovarian carcinoma patients with high alpha-folate receptor had reducing survival and cytotoxic chemo-response, *Mol. Oncol.*, 2012, **6**(3), 360–369.

